Low-impulse blast behavior of fibre-metal laminates

T.P. Vo*, Z.W. Guan, W.J. Cantwell, G.K. Schleyer

School of Engineering, University of Liverpool, Brownlow Street, Liverpool L69 3GQ, UK.

Abstract

This paper presents three dimensional (3D) finite element (FE) models of the low-impulse localised blast loading response of fibre-metal laminates (FMLs) based on an 2024-O aluminium alloy and a woven glass-fibre/polypropylene composite (GFPP). A vectorized user material subroutine (VUMAT) is developed to define the mechanical constitutive behaviour and Hashin's 3D failure criteria incorporating strain-rate effects in the GFPP. In order to apply localised blast loading, a user subroutine VDLOAD is used to model the pressure distribution over the exposed area of the plate. These subroutines are implemented into the commercial finite element code ABAQUS/Explicit to model the deformation and failure mechanisms in FMLs. The FE models consider FMLs based on various stacking configurations. Both the transient and permanent displacements of the laminates are investigated. Good correlation is obtained between the measured experimental and numerical displacements, the panel deformations and failure modes. By using the validated models, parametric studies can be carried out to optimise the blast resistance of FMLs based on a range of stacking sequences and layer thicknesses.

Keywords: Fibre-metal laminates; localised blast loading; Hashin's 3D failure criteria; strain-rate effects; finite element models

1. Introduction

Fibre-metal laminates represent an interesting type of hybrid material, formed from the combination of a metal, typically an aluminium alloy, and a fibre-reinforced composite, such as a glass fibre reinforced epoxy. Currently, GLARE (a glass fibre/aluminium) is being used by a number of aircraft manufacturers in the design of primary aircraft components. For example, the aramid fibre/epoxy system, ARALL, is presently being used in the manufacture of the cargo door of the American C-17 transport aircraft whilst GLARE is being used in the manufacture of the upper fuselage of the A380, an aircraft that is capable of carrying up to 700 passengers. Research work has shown that FMLs combine the superior durability characteristics of met-

*Corresponding author, tel.: +44 151 7945095; fax: +44 151 7945218
Email address: thucvp@liverpool.ac.uk, thucvp@gmail.com (T.P. Vo)

als with the attractive fatigue and fracture properties of fibre-reinforced composite materials ([1]-[5]). Fleischer [6] investigated the blast resistance of an FML luggage container based on a design similar to that currently used by the civil air transport sector. The FML container comfortably contained a Lockerbie-type explosion, highlighting the enormous potential offered by these structures. Unfortunately, the increased cost associated with the manufacture of these structures has limited their more widespread use in this safety-critical environment. The blast resistance of FMLs based on a 2024-O aluminium alloy and a glass fibre reinforced polypropylene subjected to localised blast loading has been investigated in earlier studies ([7]-[9]). Tests were conducted on FMLs based on twelve different stacking configurations, offering total laminate thicknesses up to 15 mm. When expressed in terms of non-dimensional parameters, the front and back face panel displacements fell within one plate thickness, following a linear trend line, and the threshold impulse for the onset of tearing was shown to be linearly dependent on panel thickness. Testing the blast response of FMLs is very time consuming, in addition to material and manpower costs. When conducting experimentally-based research, tests should cover as many scenarios as possible, such as stacking configurations, materials, geometries, loading and boundary conditions, etc. Therefore, the optimisation process is likely to be very expensive and hugely time consuming. In contrast, the development of computer models using FE analyse is a relatively quick and inexpensive process, especially in cases where there is access to supercomputer facilities. In such circumstances, only a limited number of material tests and structural blast tests are required for validation purposes. Once computer models are verified against typical blast tests, covering both the upper and lower bound cases, systematically-designed parametric studies can be undertaken using validated numerical models. Blast is an extreme dynamic loading process and to model the blast behaviour of FMLs, the mechanisms of the build up blast pressure need to be modelled in the first instance. The focus of this study concerns external blast, due to high explosives. In most blast studies, the negative phase of the blast wave is ignored, and only the parameters associated with the positive phase are considered, since it is generally accepted that the damage to the structure is caused by the positive phase. During blast, unlike metallic components, which can yield and dissipate energy via plasticity, composites can only dissipate energy by various damage or fracture processes. Therefore, an advanced modelling tool, which is capable of modelling such extreme loading cases, needs to be developed. To date, much work has been undertaken relating to sandwich and composite plates/shells subjected to blast loading and only few are mentioned herein. However, much of this work compares FE simulations with analytical solutions based on idealised assumptions or simply makes pure numerical predictions. Prusty and Satsangi [10] used a modified approach

to develop a numerical transient dynamic analysis for laminated stiffened shells. Turkmen [11] used Love's theory of thin elastic shells and FE modelling to simulate the blast response of laminated cylindrical shells. The results were compared with experimental data, in terms of blast pressure and strain-time history. Xue and Hutchinson [12] conducted a preliminary assessment of sandwich plates subject to blast loads. They suggested that sandwich plates with sufficiently strong cores had the potential to sustain substantially larger uniform impulses than solid plates of the same material and weight. Qiu et al. [13] developed an analytical model for the deformation response of clamped circular sandwich plates subjected to shock loading in air and in water. An explicit finite element method was employed to assess the accuracy of the analytical formulae for the simplified case where the effects of fluid-structure interaction were neglected. Zhu et al. [14] implemented a micro-mechanics model into ABAQUS/Explicit to undertake parametric studies of the transient responses of composite plates by varying geometry, ply stacking sequence, material models, boundary conditions and loadings. Batra and Hassan [15] analyzed 3D transient deformations of unidirectional fiber reinforced composites subjected to a blast load by the finite element method. Dolce et al. [16] conducted test and verified via simulations of fully clamped rectangular steel and CFRP targets subjected to C-4 blast loads using the commercial finite element code LS-DYNA. Fatt and Pothula [17] studied dynamic pulse buckling of laminated cylindrical shells subjected to uniform overpressure and asymmetric pressure pulse. To date, there is very limited numerical work published on the blast behaviour of FMLs. Kotzakolios et al. [18] investigated the blast response of a typical commercial fuselage for two material configurations, aluminium and GLARE, using LS-DYNA. By using ABAQUS/Explicit, Karagiozova et al. [19] investigated the blast resistant capabilities and interpreted the deformation and failure mechanisms of FML panels under highly localised blast loading. The analysis was restricted to the debonding and failure of the aluminium layers while damage inside the composite layer was not considered. Moreover, this work focused mainly on the residual deformation of the FML panels, while the elastically-driven change of shape upon unloading was not emphasized. It is clear that damage inside the GFPP blocks under localised blast loading cannot be modelled directly using the damage models available in ABAQUS due essentially to the 3D deformation process involving large transverse compression and strain-rate sensitivity. This complicated problem is not well-investigated and there is a need for further investigation in this area.

In this paper, Hashin's 3D failure criteria incorporating strain-rate effects in the GFPP and localised blast loading are implemented into the commercial finite element code ABAQUS/Explicit. The analysis is restricted to low-impulse blast behavior, which is defined here according to Mode

I failure from the experimental study carried out by Langdon et al. ([7]-[9]). This mode is defined to correspond a large inelastic deformation of the back face of the panel. The FE models cover FML panels with different lay-ups. Both the transient and permanent displacements of the laminates are investigated. Good correlation is obtained between the measured experimental and numerical displacements, the panel deformations and failure modes. By using the validated models, parametric studies can be carried out to optimise the blast resistance of FMLs based on a range of stacking sequences and layer thicknesses.

2. Geometric and loading conditions of FML panels

The response of FML panels subjected to localised blast loading carried out in the experimental study by Langdon et al. ([7]-[9]) and is investigated in this study. These 400×400 mm panels (300×300 mm exposed area), were manufactured at the University of Liverpool from sheets of 0.025 in. (approximately 0.6 mm) thick 2024-O aluminium alloy and a woven glass-fibre/polypropylene composite. The FML panels are identified using the notation, AXTYZ-#, which is described in [7], where A = aluminium, X = number of aluminium layers, T = GFPP, Y = number of blocks of GFPP, Z = number of plies of GFPP per block and # indicates the panel number. The panels were tested at the University of Cape Town using a ballistic pendulum facility. Details of the lay-ups and blast pressures investigated in this study are listed in Table 1. In order to promote better adhesion to the composite material, a thin layer of polypropylene (PP) film (Xiro 23.101) was placed between the chromate-coated aluminium alloy and the glass fibre reinforced PP composite. This is shown in Fig. 1 where a schematic arrangement of a 2/1 FML is presented. Previous work has shown that the incorporation of such a coating introduces a rough porous structure onto the surface of the alloy into which the low viscosity PP adhesive can flow when heat and pressure are applied ([3],[4]). The use of this treatment and interlayer can result in interfacial fracture energies in excess of 2000 J/m^2 [5].

3. Material modelling

ABAQUS/Explicit ([20],[21]) was used to develop numerical simulations of the various FML panels subjected to localised blast loading. Three materials need to be considered, i.e. the 2024-O aluminium alloy, the woven glass-fibre/polypropylene composite and the adhesive. Clearly, all three materials behave very differently. Therefore, different constitutive models and failure criteria are required to simulate their behaviour.

3.1. Aluminium layers

The aluminium was modeled as an elasto-plastic material exhibiting a rate-dependent behaviour. The strain-rate decomposition can be written as:

$$d\epsilon = d\epsilon_{el} + d\epsilon_{pl} \tag{1}$$

For a rate-dependent material, the relationship follows the definition of the uniaxial flow rate as:

$$\dot{\epsilon}_{pl} = h(q, \bar{\epsilon}_{pl}, \theta) \tag{2}$$

where h is a known function, q is the equivalent stress, $\bar{\epsilon}_{pl}$ is the equivalent plastic strain and θ is the temperature.

The plastic strain can be calculated as follows:

$$\epsilon_{pl} = \epsilon_{\text{total}} - \frac{\sigma_{\text{total}}}{E}, \sigma > \sigma_y \tag{3}$$

If isotropic hardening is defined, the yield stress can be given as a tabular function of plastic strain. For the 2024-O aluminium alloy used in this research, the isotropic hardening data are given in Table 2. The yield stress for a given state can be readily obtained from this table of data, and it remains constant until the plastic strain reaches the next value. The rate-dependent hardening curves, in terms of the static relation can be expressed as:

$$\bar{\sigma}\left(\bar{\epsilon}_{pl}, \dot{\bar{\epsilon}}_{pl}\right) = \sigma_y\left(\bar{\epsilon}_{pl}\right) R\left(\dot{\bar{\epsilon}}_{pl}\right) \tag{4}$$

where $\bar{\epsilon}_{pl}$ and R are the equivalent plastic strain and a stress ratio, which are:

$$\bar{\epsilon}_{pl} = \int_0^t \sqrt{\frac{2}{3}\dot{\epsilon}_{pl} : \dot{\epsilon}_{pl}}\, dt \tag{5a}$$

$$R = \bar{\sigma}/\sigma_y \tag{5b}$$

Both shear failure and tensile failure are used to simulate the failure mechanisms in the aluminium layers in the FML panels. The former is based on the value of the equivalent plastic strain at the element integration points; and failure is assumed to occur when the damage parameter δ_{sh} exceeds 1. δ_{sh} is defined as:

$$\delta_{sh} = \sum \left(\frac{\Delta \bar{\epsilon}_{pl}}{\left(\bar{\epsilon}_{pl}\right)_f} \right) \tag{6}$$

$\left(\bar{\epsilon}_{pl}\right)_f$ is the strain at failure, which must be determined experimentally. When the shear failure criterion is met at an integration point, all the stress components will be set to zero and

that material point fails. If all of the material points at any one section of an element fail, the element is removed from the mesh. The tensile failure criterion assumes that failure occurs when the pressure stress p becomes more tensile than the specified hydrostatic cut-off stress $\sigma_{\text{cut-off}}$, i.e.:

$$p = \frac{1}{3}|\sigma_{ii}| > \sigma_{\text{cut-off}} \tag{7}$$

In this criterion, the hydrostatic pressure stress is used as a measure of failure to model dynamic spall or a pressure cut-off. The element removal mechanism is similar to that offered by the shear failure criterion. The hydrostatic cut-off stress is set to 279 MPa. The Young's modulus, Poisson's ratio and density are taken as $E = 73.1$ MPa, ν=0.3 and ρ=2690 kg/m^3, respectively.

3.2. Glass fibre reinforced composite layers

Failure criteria for laminated composites are available in ABAQUS/Explicit, however they can only be applied for continuum shell elements. Further, none of these criteria consider strain-rate effects in the composite material, which is considered in the present study. The continuum shell elements, with the existing failure criteria, are not capable of taking large through-the-thickness rate-dependent deformations into account. Therefore, it is necessary to develop a constitutive model and failure criteria suitable for simulating the composite layers using 3D solid elements. For this purpose, a 3D rate-dependent failure criteria for a unidirectional composite is developed by modifying Hashin's 3D failure criteria [22], to include rate-dependent elastic moduli and strength properties. The failure criteria, with the related constitutive model, are implemented into ABAQUS/Explicit using a VUMAT subroutine provided by ABAQUS [20].

3.2.1. Constitutive models for an undamaged and a damaged laminate

Prior to damage initiation, the GFPP layer is modelled as an orthotropic elastic material. The stress-strain relations can be written as:

$$\begin{bmatrix} \sigma_{11} \\ \sigma_{22} \\ \sigma_{33} \\ \sigma_{12} \\ \sigma_{23} \\ \sigma_{31} \end{bmatrix} = \begin{bmatrix} C^0_{11} & C^0_{12} & C^0_{13} & 0 & 0 & 0 \\ C^0_{12} & C^0_{22} & C^0_{23} & 0 & 0 & 0 \\ C^0_{13} & C^0_{23} & C^0_{33} & 0 & 0 & 0 \\ 0 & 0 & 0 & C^0_{44} & 0 & 0 \\ 0 & 0 & 0 & 0 & C^0_{55} & 0 \\ 0 & 0 & 0 & 0 & 0 & C^0_{66} \end{bmatrix} \begin{bmatrix} \epsilon_{11} \\ \epsilon_{22} \\ \epsilon_{33} \\ \epsilon_{12} \\ \epsilon_{23} \\ \epsilon_{31} \end{bmatrix} \tag{8}$$

Nine independent undamaged elastic constants are defined by:

$$C^0_{11} = E_1(1-\nu_{23}\nu_{32})\Gamma \tag{9a}$$

$$C^0_{22} = E_2(1-\nu_{13}\nu_{31})\Gamma \tag{9b}$$

$$C^0_{33} = E_3(1-\nu_{12}\nu_{21})\Gamma \tag{9c}$$

$$C^0_{12} = E_1(\nu_{21}+\nu_{31}\nu_{23})\Gamma \tag{9d}$$

$$C^0_{23} = E_2(\nu_{32}+\nu_{12}\nu_{31})\Gamma \tag{9e}$$

$$C^0_{13} = E_1(\nu_{31}+\nu_{21}\nu_{32})\Gamma \tag{9f}$$

$$C^0_{44} = G_{12} \tag{9g}$$

$$C^0_{55} = G_{23} \tag{9h}$$

$$C^0_{66} = G_{13} \tag{9i}$$

$$\Gamma = 1/(1-\nu_{12}\nu_{21}-\nu_{23}\nu_{32}-\nu_{13}\nu_{31}-2\nu_{21}\nu_{32}\nu_{13}) \tag{9j}$$

where E_i is the Young's modulus in i direction, G_{ij} is shear modulus in $i-j$ plane and ν_{ij} is Poisson's ratio for transverse strain in the j-direction, when the stress is in the i-direction.

Damage initiation, which refers to the onset of degradation at a material point, is modelled based on Hashin's 3D failure criterion. Failure indices for the criteria are related to fiber and matrix failures and involve four failure modes. The damage variables associated with fiber/matrix failure in tension/compression are instantaneously set to unity when the corresponding failure criterion is satisfied. The following generalization of Hashin's quadratic failure criteria can be expressed as follows:

Tensile fibre mode: $\sigma_{11} > 0$

$$\text{If } \left(\frac{\sigma_{11}}{X_{1t}}\right)^2 + \left(\frac{\sigma_{12}}{S_{12}}\right)^2 + \left(\frac{\sigma_{13}}{S_{13}}\right)^2 = 1,\ d_{ft} = 1 \tag{10}$$

Compressive fibre mode: $\sigma_{11} < 0$

$$\text{If } \frac{|\sigma_{11}|}{X_{1c}} = 1,\ d_{fc} = 1 \tag{11}$$

Tensile matrix mode: $\sigma_{22}+\sigma_{33} > 0$

$$\text{If } \frac{(\sigma_{22}+\sigma_{33})^2}{X^2_{2t}} + \frac{\sigma^2_{23}-\sigma_{22}\sigma_{33}}{S^2_{23}} + \frac{\sigma^2_{12}+\sigma^2_{13}}{S^2_{12}} = 1,\ d_{mt} = 1 \tag{12}$$

Compressive matrix mode: $\sigma_{22}+\sigma_{33} < 0$

$$\text{If } \left[\left(\frac{X_{2c}}{2S_{23}}\right)^2 - 1\right]\frac{(\sigma_{22}+\sigma_{33})}{X_{2c}} + \frac{(\sigma_{22}+\sigma_{33})^2}{4S^2_{23}} + \frac{(\sigma^2_{23}-\sigma_{22}\sigma_{33})}{S^2_{23}} + \frac{\sigma^2_{12}+\sigma^2_{13}}{S^2_{12}} = 1,\ d_{mc} = 1 \tag{13}$$

In the above equations,

d_{ft} and d_{fc} denote the damage variables associated with fibre tension and compression failure modes.

d_{mt} and d_{mc} denote the damage variables associated with the corresponding failure modes in the matrix.

X_{1t} denotes tensile failure strength in fibre direction.

X_{1c} denotes compressive failure strength in fibre direction.

X_{2t} denotes tensile failure strength in direction 2 (transverse to fibre direction).

X_{2c} denotes compressive failure stress in direction 2 (transverse to fibre direction).

S_{12} denotes failure shear strength in 1-2 plane.

S_{13} denotes failure shear strength in 1-3 plane.

S_{23} denotes failure shear strength in 2-3 plane.

Since a woven glass-fibre/polypropylene composite layer is produced by placing fibres in a [0°/90°] pattern, the material behaviour within the plane of the laminate is similar. In addition, there is no need to separate the fibre and resin in order to simulate the overall response of the composite ply. Therefore, the longitudinal and transverse strengths in tension and compression are assumed to be the same, as are the shear strengths. The Young's moduli, shear's moduli, Poisson's ratios and strengths of GFPP are given in Table 3.

Once damage initiation has occurred, the response of the material is similar to that predicted by Eq.(8). In this case, the damaged elastic constants, C_{ij}, are used. These constants are computed in terms of undamaged elastic constants, C^0_{ij}, and the damage variables according to:

$$C_{11} = (1-d_f)C^0_{11} \tag{14a}$$

$$C_{22} = (1-d_f)(1-d_m)C^0_{22} \tag{14b}$$

$$C_{33} = (1-d_f)(1-d_m)C^0_{33} \tag{14c}$$

$$C_{12} = (1-d_f)(1-d_m)C^0_{12} \tag{14d}$$

$$C_{23} = (1-d_f)(1-d_m)C^0_{23} \tag{14e}$$

$$C_{13} = (1-d_f)(1-d_m)C^0_{13} \tag{14f}$$

$$C_{44} = (1-d_f)(1-s_{mt}d_{mt})(1-s_{mc}d_{mc})C^0_{44} \tag{14g}$$

$$C_{55} = (1-d_f)(1-s_{mt}d_{mt})(1-s_{mc}d_{mc})C^0_{55} \tag{14h}$$

$$C_{66} = (1-d_f)(1-s_{mt}d_{mt})(1-s_{mc}d_{mc})C^0_{66} \tag{14i}$$

where the global fibre and matrix damage variables are also defined as:

$$d_f = 1 - (1 - d_{ft})(1 - d_{fc}) \tag{15a}$$

$$d_m = 1 - (1 - d_{mt})(1 - d_{mc}) \tag{15b}$$

The factors s_{mt} and s_{mc} in the definitions of the shear moduli are introduced to control the reduction in shear stiffness caused by tensile and compressive failure in the matrix respectively. The following values were recommended by ABAQUS [20]: $s_{mt} = 0.9$ and $s_{mc} = 0.5$.

3.2.2. Strain-rate dependent model

Based on the work by Yen and Caiazzo ([23],[24]) and Daniel et al. [25], strain-rate effects are included by using logarithmic functions in the six elastic moduli in Eq.(9) and the strength values in Eqs.(10-13). The strain-rate equation for the strength values is given by:

$$\{S_{RT}\} = \{S_0\} \left(1 + C_1 \ln \frac{\dot{\bar{\epsilon}}}{\dot{\epsilon}_0}\right) \tag{16}$$

where:

$$\{\dot{\bar{\epsilon}}\} = \left\{|\dot{\epsilon}_1| \quad |\dot{\epsilon}_2| \quad |\dot{\epsilon}_1| \quad |\dot{\epsilon}_2| \quad |\dot{\epsilon}_{12}| \quad |\dot{\epsilon}_{13}| \quad |\dot{\epsilon}_{23}|\right\}^T \tag{17}$$

$$\{S_{RT}\} = \left\{X_{1t} \quad X_{2t} \quad X_{1c} \quad X_{2c} \quad S_{12} \quad S_{13} \quad S_{23}\right\}^T \tag{18}$$

and C_1 is the strain-rate constant and $\{S_0\}$ are the strength values of $\{S_{RT}\}$ at the reference strain-rate $\dot{\epsilon}_0 = 1\text{s}^{-1}$.

Strain-rate effects in the elastic moduli are similar to Eq.(16):

$$\{E_{RT}\} = \{E_0\} \left(1 + C_2 \ln \frac{\dot{\bar{\epsilon}}}{\dot{\epsilon}_0}\right) \tag{19}$$

where:

$$\{\dot{\bar{\varepsilon}}\} = \left\{|\dot{\varepsilon}_1| \quad |\dot{\varepsilon}_2| \quad |\dot{\varepsilon}_3| \quad |\dot{\varepsilon}_{12}| \quad |\dot{\varepsilon}_{13}| \quad |\dot{\varepsilon}_{23}|\right\}^T \tag{20}$$

$$\{E_{RT}\} = \left\{E_1 \quad E_2 \quad E_3 \quad G_{12} \quad G_{13} \quad G_{23}\right\}^T \tag{21}$$

and C_2 is the strain-rate constant and $\{E_0\}$ are the elastic moduli of $\{E_{RT}\}$ at the reference strain-rate.

3.2.3. Implementation of the material model in a user material subroutine

The flowchart of the VUMAT subroutine used to implement the material model and failure criteria described in the previous sections is given in Fig. 2. In the flowchart, *nblock* is a term

used in ABAQUS that refers to the number of integration points to be processed, once the subroutine is called. This subroutine is complied and linked with the finite element solver and enables ABAQUS/Explicit to obtain the required information regarding the state of the material and the material mechanical response during each time step, for each integration point of each element. The stresses in the material coordinate system are computed within the VUMAT subroutine using the given strains and the material stiffness coefficients at each material point. Having these stresses, the Hashin's 3D failure criteria outlined in Eqs.(10-13) are calculated, and the elastic modulus and strength values are adjusted for strain-rate effects using Eqs.(16) and (19). When an element fails as determined by the failure model, the element status is then changed from 1 to 0. At this point, the stresses at the material point are reduced to zero and it no longer contributes to the model stiffness. When all of the material status points of an element have been reduced to zero, the element is removed from the mesh. The implementation process for the 3D solid elements follows the steps below:

(a) Call a VUMAT subroutine with the previous strain vector as well as the iterative increment in strains, and trial values for the constitutive matrix at this material point.

(b) Update the total elastic strain for this iteration by summing the total strains from the previous increment and the corresponding iterative increments of strain.

(c) Compute the strain-rate and adjust the elastic moduli.

(d) Compute the updated stresses using the constitutive matrix and the total strains at this material point as well as adjust the strength values.

(e) Perform the failure initiation check using the Hashin's 3D failure criteria with adjusted elastic modulus and strength values in previous steps and determine whether any material failure had initiated. If so, perform the material degradation step.

(f) Perform the material degradation step. If material failure is detected, then degrade the material properties by degrading the entries in the constitutive matrix, so that the appropriate stress component will approach zero after failure initiation.

(g) Re-compute the constitutive matrix and the stresses, update the solution-dependent variables, and return to ABAQUS.

3.3. Cohesive material properties

The cohesive element, defined in terms of traction-separation, was used to mesh the adhesive layer. The traction-separation model in ABAQUS assumes an initially linear elastic behaviour, followed by initiation and evolution of damage. The elastic behaviour of the element is written in terms of the elastic constitutive matrix that relates the nominal stress to the nominal strain.

The uncoupled traction-separation behaviour, as presented in Eq.(22), was used:

$$t = \begin{Bmatrix} t_n \\ t_s \\ t_t \end{Bmatrix} = \begin{bmatrix} K_{nn} & 0 & 0 \\ 0 & K_{ss} & 0 \\ 0 & 0 & K_{tt} \end{bmatrix} \begin{Bmatrix} \epsilon_n \\ \epsilon_s \\ \epsilon_t \end{Bmatrix} = K\epsilon \tag{22}$$

where t is the nominal traction stress vector, K is the elastic constitutive stiffness matrix and ϵ is the nominal strain vector. The default choice of the constitutive thickness for modeling the response, in terms of traction versus separation, is 1.0, regardless of the actual thickness of the cohesive layer. Thus, the elastic constitutive stiffness matrix and density should be calculated using the true thickness of the cohesive layer t_c as $K = E/t_c$ and $\rho = \rho_c t_c$.

A quadratic nominal stress criterion, as shown in Eq.(23), was used as the damage initiation criterion of the cohesive layer:

$$\left\{ \frac{\langle t_n \rangle}{t_n^0} \right\}^2 + \left\{ \frac{\langle t_s \rangle}{t_s^0} \right\}^2 + \left\{ \frac{\langle t_t \rangle}{t_t^0} \right\}^2 = 1 \tag{23}$$

where: t_n, t_s and t_t are the current normal stress and shear stresses of the cohesive element and t_n^0, t_s^0 and t_t^0 are the corresponding critical nominal normal stress and shear stresses, respectively.

Damage evolution was defined based on the energy conjunction with the linear softening law. This criterion can be represented as:

$$\left\{ \frac{G_n}{G_n^c} \right\} + \left\{ \frac{G_s}{G_s^c} \right\} + \left\{ \frac{G_t}{G_t^c} \right\} = 1 \tag{24}$$

where G_n, G_s and G_t refer to the work done by the traction and its conjugate separation in the normal, the first, and the second shear directions; G_n^c, G_s^c and G_t^c refer to the critical fracture energies required to cause failure in the normal, the first, and the second shear directions, respectively.

In the above expressions, Eqs.(22-24), the mechanical properties of cohesive elements were obtained from Karagiozova et al. [19], and the resultant strength, stiffness, and fracture energy values for the interface are given in Table 4.

4. Finite element modelling

4.1. Mesh and interaction, constraint conditions between components

The calculation time can be reduced by using the inherent symmetry of the problem. Thus, only a quarter of each FML panel was modeled with the appropriate boundary conditions applied along the planes of symmetry. The mesh generation, dimensions, loading and boundary

conditions for typical FML panel (A3T28) are shown in Fig. 3. The 3D panel is comprised of the aluminium, the composite and the cohesive layers as separate parts. The aluminium and composite plates were meshed using C3D8R elements, which are eight-noded, linear hexahedral elements with reduced integration and hourglass control. Such elements are capable of accurately capturing the stresses and strains. The individual aluminium and composite plies were discretized with two elements through the thickness. The interface between these two layers were created with the eight-noded 3D cohesive elements (COH3D8). Since the principal region of interest was the central area, an irregular mesh was generated, with a biased mesh seeding along the edges towards the target center. Mesh sensitivity studies were conducted, which demonstrated the satisfactory accuracy of the numerical results and mesh convergence rate, when a central area of 60×60 mm was meshed using an in-plane element size of 1×1 mm. A condition of general contact interaction was defined between the two neighbouring layers of aluminum and composite. Surface-based tie constraints were imposed between either the aluminum or the composite layer and the cohesive layer to model adhesion between the adjacent layers. The contact interaction properties for interaction between the aluminium and composite layer, as well as between either the aluminum or composite layer and the cohesive layer, were also defined.

4.2. Boundary conditions and localised blast loading

Due to the symmetric nature of the FML panels, symmetric boundary conditions were applied to the nodes lying on XY and YZ plane, as shown in Fig. 3. The other two edges were fully fixed. In order to apply localised blast loading in ABAQUS, the load is assumed to act impulsively and is applied using a pressure load acting on the exposed face of FML panels. Details of the localised blast loading and loading model validation can be found elsewhere ([19] and [26]). The pressure loading $P(r,t)$ is a function of both time and distance from the plate centre and is given by:

$$P(r,t) = p_1(r)p_2(t) \tag{25}$$

where:

$$p_1(r) = \begin{cases} P_0 & r \leq r_0 \\ P_0 e^{-k(r-r_0)} & r_0 < r < r_b \\ 0 & r > r_b \end{cases} \tag{26a}$$

$$p_2(t) = e^{-2t/t_0} \tag{26b}$$

In Eq.(26), $r_0 = 15$ mm is the radius of the explosive disc used in the experiments, $r_b < L/2$, L is the length of the panel and $t_0 = 0.008$ms is the characteristic decay time for the pulse and

k is an exponential decay parameter. In this study, this decay parameter is not constant, but a function of the total impulse (Ref.[19]). The total impulse is defined as:

$$I = 2\pi \int_0^{\infty} \int_0^{r_b} P(r,t) dr dt \tag{27}$$

A user subroutine VDLOAD was used to model the pressure distribution over the exposed area of the plate. This subroutine allows the user to define the load as a function of position and time. The peak pressure P_0 was calculated from the measured impulse using Eqs.(25) and (27) and the values are given in Table 1.

5. Results and discussion

The FE models, using the constitutive models and failure criteria presented in the previous sections, were developed to simulate the blast behavior of FML panels based on various lay-ups. Initially, two FML panels, A3T28-4 and A4T32-4, were studied to identify an appropriate strain-rate material model for the composite layer and to investigate the transient response. By examining these panels, the FE models can be partly verified. It should be noted that for the woven glass-fibre/polypropylene composite, there are no experimental data available in the literature to describe strain-rate effects. In this study, different values of the strain-rate constant were investigated, and those values that agreed well with the experimental results were $C_1 = 0.35$ and $C_2 = 0.35$. To investigate the rate-dependent material model in more details, six models were considered, and these were as follows:

1. No strain-rate effects, i.e. the strength and elastic modulus values are those obtained from the static material tests.
2. Strain-rate effects in the strength values only, i.e. the elastic modulus values are those obtained from the static material tests.
3. Strain-rate effects in the strength and shear modulus values, i.e. the Young's modulus values are those obtained from the static material tests.
4. Strain-rate effects in the strength and elastic modulus values.
5. Strain-rate effects in the strength and the through-thickness modulus values.
6. Strain-rate effects in the strength, shear and the through-thickness modulus values.

After conducting a number of convergence studies, numerical simulations were carried out over a time period of 4 ms. The mid-point deflections for the front and back faces of panels A3T28-4 and A4T32-4, along with experimental results are given in Table 5. The transient displacement, which is not evident in the experimental data, is also given by the ABAQUS/Explicit

simulation. As shown in the rightmost column, the differences between the calculated and experimental permanent displacements are large for Cases 1-4, but decreases significantly for Cases 5 and 6. When strain-rate effects are not correctly considered, the permanent displacements are over-estimated, especially for the front face, since some GFPP elements are deleted, as shown in Fig. 4. It can be seen from Table 5 and Fig. 5 that good agreement is observed between the experimentally-measured deflections, the deformation mode and those values obtained from the FE model using Case 6. Thus, the remainder of the study is based on this particular material model. This is consistent with experimental results of McCarthy et al. [27] on the strain-rate sensitivity of glass-fibre FMLs and the numerical modelling study of Gama and Gillespie [28] on the impact behaviour of thick-section composites. In their research, no strain-rate effects were taken into account for the in-plane elastic moduli E_1 and E_2 of the composite layers. To investigate strain-rate effects further, using Cases 5 and 6, the variation of the front and back displacements with time for panels A3T28-4 and A4T32-4 are illustrated in Fig. 6. Due to the small impulse, there is a large elastic regime in the dynamic response. The displacements obtained using Case 6 are less than those obtained using Case 5. This can be explained as follows. When strain-rate effects in the shear moduli and the through-thickness modulus are considered simultaneously (Case 6), these moduli increase with an increase in the effective strain-rate. Therefore, the effect on the shear stresses is enhanced, resulting in a reduced central deflection. This indicates that the material model in Case 5 is less stiff than that in Case 6. Figure 7 shows frames after 0.52 ms and 0.60 ms when panels A3T28-4 and A4T32-4 almost reach the maximum transient displacement. The time histories of the energies for these panels were determined and are shown in Fig. 8. The total work done (ALLWK) corresponds to the amount of energy applied to the system. This work is converted into different types of energy: kinetic energy (ALLKE) related to inertia and internal energy (ALLIE) of FML panels. The internal energy includes energy stored in the material due to linear elastic strains (ALLSE), energy dissipated (ALLPD) to cause permanent deformation, due to plastic strains of aluminum layers. The total energy is found to remain almost constant during the analysis, as expected. The kinetic energy (ALLKE) and elastic strain energy (ALLSE) increase and reach maximum values at an early stage, and then, decrease. In contrast, the internal energy (ALLIE) and plastic dissipation energy (ALLPD) increase from zero and exhibit small oscillations before reaching the maximum values after 2ms. Finite element models of other types of FML panels subjected to a low impulse were also developed to broaden the validation. The experimental and numerical results are presented in Table 6. **Reasonable agreement between the predicted and experimental mid-point displacements was observed, most particularly in the**

back face displacements. The response of the front face is not correctly predicted. This is possibly due to the failure of FE model to accurately capture the front face buckling failure immediately adjacent to the edge of the blast area. A comparison of the total work done (ALLWK) and the plastic dissipation (ALLPD) indicates that most of the work done by the blast load is dissipated in plastic deformation of the aluminum layers. For a given panel configuration, the back and front face displacements increase with increasing impulse. For a particular impulse, thinner panels exhibit higher displacements than thicker ones, as expected. Comparing the experimental and numerical failure modes of five typical panels, as shown in Fig. 9, the simulations capture most of the details of the failure mechanisms. These include debonding of the front face (A2T28-4, Fig. 9a), back face, debonding and local buckling of the internal aluminium layer (A4T34-3, Fig. 9b). The thin panels (A2T18-4, A4T32-4 and A5T42-2) deformed with a small amount of debonding on the back face. The thick panels (A3T28-4, A4T34-3, A4T36-2 and A4T38-2), contain thicker GFPP blocks, have larger bending stiffnesses than their thinner counterparts and tend to exhibit greater local buckling of the internal aluminium layer.

To investigate the blast response of the FMLs further, the quantitative analysis of experimental and numerical data is presented. The results are used to quantify the relationship in a non-dimensional form between the impulse and the displacement for both the front and back faces. In this study, the same approach suggested by Langdon et al. ([8],[29]) was adopted. Here, the non-dimensional impulse and displacements are given by:

$$\Phi_q = \frac{I(1+\ln\frac{BL}{\pi r_0^2})}{2t^2\sqrt{BL\rho\sigma}} \tag{28a}$$

$$\delta_F = \frac{d_F}{t} \tag{28b}$$

$$\delta_B = \frac{d_B}{t} \tag{28c}$$

where ρ: material density, B, L: plate width and length, t: plate thickness and σ: characteristic material stress. Values for this stress were calculated using a rule of mixtures approximation, similar to that adopted by Lemanski et al. [8].

The non-dimensional front and back displacements of the FML panels are calculated and plotted against the non-dimensional impulse in Figs. 10 to 12. As expected, there is a linear relationship between the non-dimensional displacement and the non-dimensional impulse for the front and back faces. The permanent displacements correlate reasonably well with the experimental results, especially when the back face is considered. The transient data from the FE models in Fig 12 indicate that the front face displacement will always be smaller than that

of back face. As the non-dimensional impulse increases, the back face displacement increases more rapidly than that of front face.

The trend-line equations for the front face non-dimensional displacement are given by:

$$\text{Transient displacement (FE): } \delta_F = 0.62\Phi_q + 0.29, R^2 = 0.90 \tag{29a}$$

$$\text{Permanent displacement (FE): } \delta_F = 0.52\Phi_q - 0.30, R^2 = 0.81 \tag{29b}$$

$$\text{Permanent displacement (experiment): } \delta_F = 0.85\Phi_q - 0.60, R^2 = 0.89 \tag{29c}$$

and for the back face:

$$\text{Transient displacement (FE): } \delta_B = 0.88\Phi_q + 1.08, R^2 = 0.95 \tag{30a}$$

$$\text{Permanent displacement (FE): } \delta_B = 0.78\Phi_q + 0.68, R^2 = 0.93 \tag{30b}$$

$$\text{Permanent displacement (experiment): } \delta_B = 0.78\Phi_q + 0.78, R^2 = 0.89 \tag{30c}$$

Although only a crude curve-fitting procedure, data in this form could potentially be used for estimating the blast response of other stacking sequences beyond those considered here.

6. Conclusions

A number of full 3D finite element models of FML panels based on a 2024-O aluminium alloy and a woven glass-fibre/polypropylene composite subjected to low-impulse localised blast loading are developed and validated against published experimental data. Hashin's 3D failure criteria, incorporating strain-rate effects in the GFPP and localised blast loading are implemented into the commercial finite element code ABAQUS/Explicit. The FE models cover FML panels with different stacking configurations. The effects of strain-rate on the transient and permanent displacements of the FML panels are investigated. The material model, which includes strain-rate effects in the strength, shear moduli, and the through-thickness modulus, is found to provide sufficiently accurate simulations of the experimental results. Deformation modes and failure mechanisms, such as debonding of the front face, back face, debonding and buckling of the internal aluminium layer, are captured by the simulations. Using non-dimensional impulse - displacement relationships, it has been shown that the simulated data correlate reasonably well with previously-published experimental results, most particularly in the terms of back face displacements.

7. Acknowledgments

The authors would like to thank the UK Leverhulme Trust for the financial support for the work presented in this paper. The authors also would like to acknowledge the use of the

UK National Grid Service in carrying out this work. The first author would like to thank Dr. Benjamin Hagege, Dr. Jake Hundley and Dr. Gautam Gopinath for their discussion about VUMAT subroutine.

8. References

References

[1] S. Krishnakumar, Fibre metal laminates-the synthesis of metals and composites, Materials and Manufacturing Processes 9 (2) (1994) 295–354.

[2] L. B. Vogelesang, A. Vlot, Development of fibre metal laminates for advanced aerospace structures, Journal of Materials Processing Technology 103 (1) (2000) 1 – 5.

[3] G. Reyes-Villanueva, Processing and characterisation of the mechanical properties of novel fibre-metal laminates, Ph.D. thesis, The University of Liverpool, Department of Engineering (2002).

[4] G. Reyes-Villanueva, W. J. Cantwell, The high velocity impact response of composite and FML-reinforced sandwich structures, Composites Science and Technology 64 (1) (2004) 35 – 54.

[5] G. Reyes, W. J. Cantwell, The mechanical properties of fibre-metal laminates based on glass fibre reinforced polypropylene, Composites Science and Technology 60 (7) (2000) 1085 – 1094.

[6] H. J. Fleisher, Design and explosive testing of a blast resistant luggage container, in: International conference on structures under shock and impact, 1996, pp. 51–60.

[7] G. S. Langdon, S. L. Lemanski, G. N. Nurick, M. C. Simmons, W. J. Cantwell, G. K. Schleyer, Behaviour of fibre-metal laminates subjected to localised blast loading: Part I–Experimental observations, International Journal of Impact Engineering 34 (7) (2007) 1202 – 1222.

[8] S. L. Lemanski, G. N. Nurick, G. S. Langdon, M. C. Simmons, W. J. Cantwell, G. K. Schleyer, Behaviour of fibre metal laminates subjected to localised blast loading–Part II: Quantitative analysis, International Journal of Impact Engineering 34 (7) (2007) 1223 – 1245.

[9] G. S. Langdon, G. N. Nurick, S. L. Lemanski, M. C. Simmons, W. J. Cantwell, G. K. Schleyer, Failure characterisation of blast-loaded fibre-metal laminate panels based on aluminium and glass-fibre reinforced polypropylene, Composites Science and Technology 67 (7-8) (2007) 1385 – 1405.

[10] B. G. Prusty, S. K. Satsangi, Finite element transient dynamic analysis of laminated stiffened shells, Journal of Sound and Vibration 248 (2) (2001) 215 – 233.

[11] H. S. Turkmen, Structural response of laminated composite shells subjected to blast loading: comparison of experimental and theoretical methods, Journal of Sound and Vibration 249 (4) (2002) 663 – 678.

[12] Z. Xue, J. W. Hutchinson, Preliminary assessment of sandwich plates subject to blast loads, International Journal of Mechanical Sciences 45 (4) (2003) 687 – 705.

[13] X. Qiu, V. S. Deshpande, N. A. Fleck, Dynamic response of a clamped circular sandwich plate subject to shock loading, Journal of Applied Mechanics 71 (5) (2004) 637–645.

[14] L. Zhu, A. Chattopadhyay, R. K. Goldberg, Nonlinear transient response of strain rate dependent composite laminated plates using multiscale simulation, International Journal of Solids and Structures 43 (9) (2006) 2602 – 2630.

[15] R. C. Batra, N. M. Hassan, Blast resistance of unidirectional fiber reinforced composites, Composites Part B: Engineering 39 (3) (2008) 513–536.

[16] F. Dolce, M. Meo, A. Wright, M. French, M. Bernabei, Structural response of laminated composite plates to blast load, Plastics, Rubber and Composites 39 (2010) 180–188.

[17] M. S. H. Fatt, S. G. Pothula, Dynamic pulse buckling of composite shells subjected to external blast, Composite Structures 92 (7) (2010) 1716 – 1727.

[18] T. Kotzakolios, D. Vlachos, V. Kostopoulos, Blast response of metal composite laminate fuselage structures using finite element modelling, Composite Structures 93 (2) (2011) 665 – 681.

[19] D. Karagiozova, G. Langdon, G. Nurick, S. C. K. Yuen, Simulation of the response of fibre-metal laminates to localised blast loading, International Journal of Impact Engineering 37 (6) (2010) 766 – 782.

[20] ABAQUS, Theory Manual, Version 6.9, Hibbitt, Karlsson & Sorensen, Inc. (2009).

[21] ABAQUS/Explicit, Users Manual, Version 6.9, Hibbitt, Karlsson & Sorensen, Inc. (2009).

[22] Z. Hashin, Failure criteria for unidirectional fiber composites, Journal of Applied Mechanics 47 (1980) 329–334.

[23] C. F. Yen, A. Caiazzo, Innovative processing of multifunctional composite armor for ground vehicles, ARL-CR-484, US Army Research Laboratory, Aberdeen Proving Ground, MD, 2001.

[24] C. F. Yen, Ballistic impact modeling of composite materials, in: Proceedings of the 7th International LS-DYNA Users Conference, Vol. 6, 2002, pp. 15–23.

[25] I. M. Daniel, B. T. Werner, J. S. Fenner, Strain-rate-dependent failure criteria for composites, Composites Science and Technology 71 (3) (2011) 357 – 364.

[26] D. Bonorchis, G. N. Nurick, The influence of boundary conditions on the loading of rectangular plates subjected to localised blast loading - Importance in numerical simulations, International Journal of Impact Engineering 36 (1) (2009) 40 – 52.

[27] M. A. McCarthy, J. R. Xiao, N. Petrinic, A. Kamoulakos, V. Melito, Modelling of bird strike on an aircraft wing leading edge made from fibre metal laminates- part 1: Material modelling, Applied Composite Materials 11 (2004) 295–315.

[28] B. A. Gama, J. W. Gillespie Jr., Finite element modeling of impact, damage evolution and penetration of thick-section composites, International Journal of Impact Engineering 38 (4) (2011) 181 – 197.

[29] G. S. Langdon, W. J. Cantwell, G. N. Nurick, The blast response of novel thermoplastic-based fibre-metal laminates - some preliminary results and observations, Composites Science and Technology 65 (6) (2005) 861 – 872.

CAPTIONS OF TABLES

Table 1: Details of the lay-ups and blast pressures investigated in this study.

Table 2: Isotropic hardening data for the 2024-O aluminium alloy.

Table 3: Properties of the GFPP layers.

Table 4: Properties of the cohesive layers.

Table 5: Experimental from Ref.[8] and numerical simulation results of transient and permanent displacements of front and back faces of panels A3T28-4 and A4T32-4 (mm).

Table 6: Summary of the experimental from Ref.[8] and numerical simulation results.

Table 1: Details of the lay-ups and blast pressures investigated in this study.

Lay-ups	No. of layers	Thickness (mm)	Impulse (Ns)	Pressure P_0 (MPa)
A2T14-2	6	3.36	5.89	844.97
A2T18-3	10	5.35	6.17	881.59
A2T18-4		5.6	7.94	1105.11
A3T22-2	7	4.09	7.57	1059.54
A3T22-4		4.13	7.7	1075.62
A3T24-5	11	6.08	10.58	1411.99
A3T24-7		6.27	3.76	555.55
A3T24-8		6.06	7.85	1094.08
A3T26-1	15	8.49	7.8	1087.94
A3T26-3		8.1	9.54	1294.99
A3T26-4		8.41	11.29	1488.88
A3T28-4	19	9.84	12.43	1607.15
A3T28-5		9.82	10.34	1385.44
A4T32-1	10	5.81	7.00	988.13
A4T32-2		5.86	4.73	689.71
A4T32-4		5.85	7.23	1017.12
A4T34-1	16	8.66	9.72	1315.60
A4T34-3		8.59	11.84	1546.74
A4T34-5		8.73	7.01	989.39
A4T36-1	22	11.53	13.70	1731.21
A4T36-2		11.48	11.61	1522.73
A4T38-2	28	13.9	11.13	1471.76
A5T42-4	13	7.46	8.87	1216.91

Table 2: Isotropic hardening data for the 2024-O aluminium alloy.

Yield stress (MPa)	76	100	113	122	150	176	183	186
Plastic strain	0	0.0074	0.0117	0.0200	0.0363	0.0700	0.1000	0.2000

Table 3: Properties of the GFPP layers.

Elastic properties									
E_1(GPa)	E_2(GPa)	E_3(GPa)	ν_{12}	ν_{13}	ν_{23}	G_{12}(GPa)	G_{13}(GPa)	G_{23}(GPa)	ρ (kg/m^3)
13.0	13.0	2.4	0.1	0.3	0.3	1.72	1.72	1.69	1800
Progressive failure									
X_{1t}(MPa)	X_{1c}(MPa)	X_{2t}(MPa)	X_{2c}(MPa)	S_{12}(MPa)	S_{13}(MPa)	S_{23}(MPa)			
300	200	300	200	140	140	140			

Table 4: Properties of the cohesive layers.

Elastic properties					Damage initiation			Damage evolution	
E_n(GPa)	E_s(GPa)	E_t(GPa)	Thickness (m)	ρ_c(kg/m^3)	t_n^0(MPa)	t_s^0(MPa)	t_t^0(MPa)	G_n^c(J/m^2)	G_s^c(J/m^2)	G_t^c(J/m^2)
2.05	0.72	0.72	10^{-4}	920	140	300	300	2000	3000	3000

Table 5: Experimental from Ref.[8] and numerical simulation results of transient and permanent displacements of front and back faces of panels A3T28-4 and A4T32-4 (mm).

Lay-ups	A3T28-4						A4T32-4					
	Transient		Permanent		Difference (%)		Transient		Permanent		Difference (%)	
	Front	Back	Front	Back	Front	Back	Front	Back	Front	Back	Front	Back
Numerical												
Case 1	23.16	25.87	16.44	20.58	301.04	22.91	22.89	23.43	19.00	19.66	37.68	14.28
Case 2	14.47	32.70	8.29	27.82	102.18	4.19	16.67	24.02	12.05	20.27	12.71	17.84
Case 3	14.72	35.56	7.11	30.84	73.33	15.51	14.84	24.63	9.74	21.04	29.42	22.31
Case 4	18.23	23.78	6.32	17.91	54.07	32.93	16.65	20.47	10.25	15.08	25.71	12.31
Case 5	13.30	29.01	5.99	23.80	46.13	10.86	16.24	22.82	11.98	18.80	13.16	9.27
Case 6	12.21	28.86	4.16	23.43	1.57	12.24	14.97	22.17	10.42	18.09	24.48	5.19
Experiment	-	-	4.10	26.70			-	-	13.80	17.20		

Table 6: Summary of the experimental from Ref.[8] and numerical simulation results.

Lay-ups	Impulse	Numerical						Experiment	
	(Ns)	Transient displ. (mm)		Permanent displ. (mm)		Energy (J)		Permanent displ. (mm)	
		Front	Back	Front	Back	ALLWK	ALLPD	Front	Back
A2T14-2	5.89	19.89	28.18	16.06	24.48	223.35	180.80	17.80	23.40
A2T18-3	6.17	12.67	20.82	6.25	15.90	164.62	142.84	6.80	13.40
A2T18-4	7.94	13.36	25.46	6.17	19.94	254.40	220.97	9.10	16.30
A3T22-2	7.57	15.22	26.54	10.88	22.54	288.97	214.86	20.40	22.20
A3T22-4	7.7	15.20	25.77	10.64	22.02	295.09	226.50	25.70	26.10
A3T24-5	10.58	14.97	28.60	5.64	22.94	395.20	270.21	16.60	26.00
A3T24-7	3.76	9.39	9.61	5.31	5.51	55.99	44.45	6.40	6.90
A3T24-8	7.85	14.70	22.39	8.20	17.39	228.97	160.04	10.10	19.30
A3T26-1	7.8	11.15	18.51	5.05	13.82	193.79	130.38	11.40	12.90
A3T26-3	9.54	12.15	23.55	4.54	18.61	290.06	186.29	7.20	23.70
A3T26-4	11.29	12.24	27.22	3.87	21.76	378.98	241.42	17.80	25.30
A3T28-4	12.43	12.21	28.86	4.16	23.43	368.13	254.87	4.10	26.70
A3T28-5	10.34	11.27	23.98	4.52	18.85	268.36	182.10	2.20	20.90
A4T32-1	7.00	14.82	21.57	10.27	17.29	175.41	137.44	12.70	16.00
A4T32-2	4.73	12.06	13.96	7.86	10.30	84.22	65.99	7.10	8.60
A4T32-4	7.23	14.97	22.17	10.42	18.09	184.57	143.60	13.80	17.20
A4T34-1	9.72	12.22	25.50	5.16	21.15	243.04	162.91	7.90	25.30
A4T34-3	11.84	13.19	30.60	5.05	26.24	350.57	237.19	7.00	28.30
A4T34-5	7.01	10.38	18.65	4.46	14.55	134.04	89.26	7.60	14.00
A4T36-1	13.70	11.03	31.68	3.70	26.48	399.38	249.36	4.70	25.60
A4T36-2	11.61	10.07	27.35	3.88	22.79	295.97	183.86	5.40	22.60
A4T38-2	11.13	6.73	25.32	1.79	19.40	252.59	140.58	4.30	20.70
A5T42-4	8.87	14.15	25.50	8.56	21.34	219.76	155.661	1.50	19.90

Figure 1: Schematic of the stacking arrangement for a 2/1 FML indicating the positioning of the PP film.

Figure 2: Flowchart for implementation of Hashin's 3D failure criteria into ABAQUS/Explicit.

Figure 3: Dimensions, loading, boundary conditions and mesh generation for typical 3/2 FML panel.

Figure 4: Deformed shapes of a panel A4T32-4 with different model of strain-rate.

Figure 5: Comparison between the experiments and numerical simulations of panels A3T28-4 and T4T32-4.

Figure 6: Front and back displacement versus time for panels A3T28-4 and A4T32-4 with two models of strain-rate.

Figure 7: Transient displacement of panels A3T28-4 and T4T32-4.

Figure 8: The time history of the energies of panels A3T28-4 and T4T32-4.

Figure 9: Comparison between the experiments and numerical simulations of panels A2T18-4, A4T34-3, A4T36-2, A4T38-2 and T5T42-4.

Figure 10: Graph of non-dimensional permanent displacement of front face versus non-dimensional impulse.

Figure 11: Graph of non-dimensional permanent displacement of back face versus non-dimensional impulse.

Figure 12: Graph of non-dimensional transient displacement of back and front face versus non-dimensional impulse.

CAPTIONS OF FIGURES

Figure 1: Schematic of the stacking arrangement for a 2/1 FML indicating the positioning of the PP film.
Figure 2: Flowchart for implementation of Hashin's 3D failure criteria into ABAQUS/Explicit
Figure 3: Dimensions, loading, boundary conditions and mesh generation for typical 3/2 FML panel.
Figure 4: Deformed shapes of a panel A4T32-4 with different model of strain-rate.
Figure 5: Comparison between the experiments and numerical simulations of panels A3T28-4 and T4T32-4.
Figure 6: Front and back displacement versus time for panels A3T28-4 and A4T32-4 with two models of strain-rate.
Figure 7: Transient displacement of panels A3T28-4 and T4T32-4.
Figure 8: The time history of the energies of panels A3T28-4 and T4T32-4.
Figure 9: Comparison between the experiments and numerical simulations of panels A2T18-4, A4T34-3, A4T36-2, A4T38-2 and T5T42-4.
Figure 10: Graph of non-dimensional permanent displacement of front face versus non-dimensional impulse.
Figure 11: Graph of non-dimensional permanent displacement of back face versus non-dimensional impulse.
Figure 12: Graph of non-dimensional transient displacement of back and front face versus non-dimensional impulse.

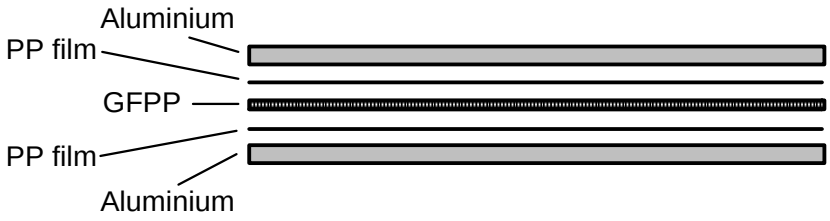

Figure 1: Schematic of the stacking arrangement for a 2/1 FML indicating the positioning of the PP film.

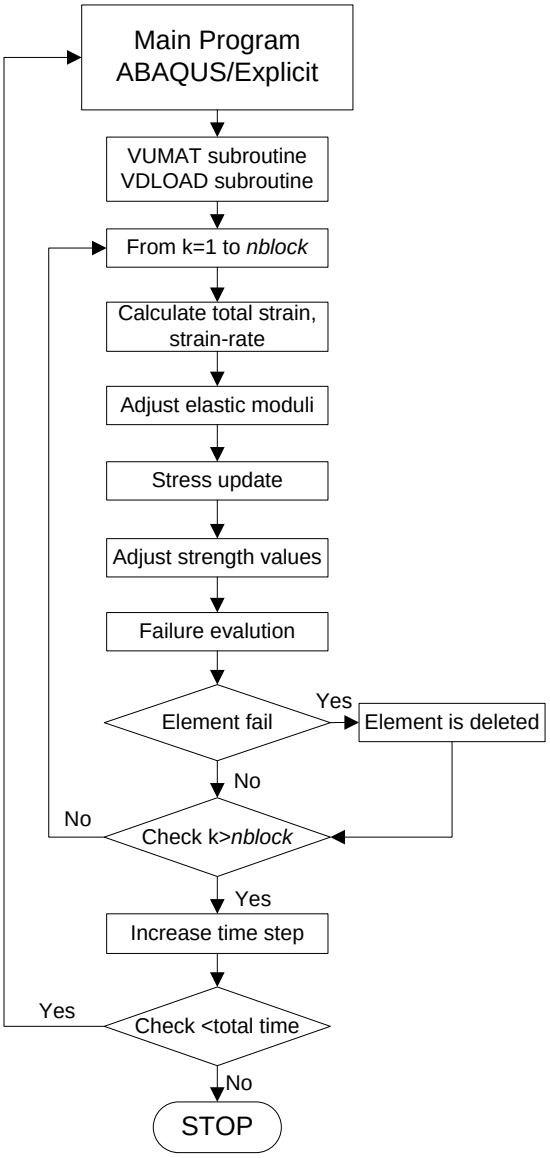

Figure 2: Flowchart for implementation of Hashin's 3D failure criteria into ABAQUS/Explicit

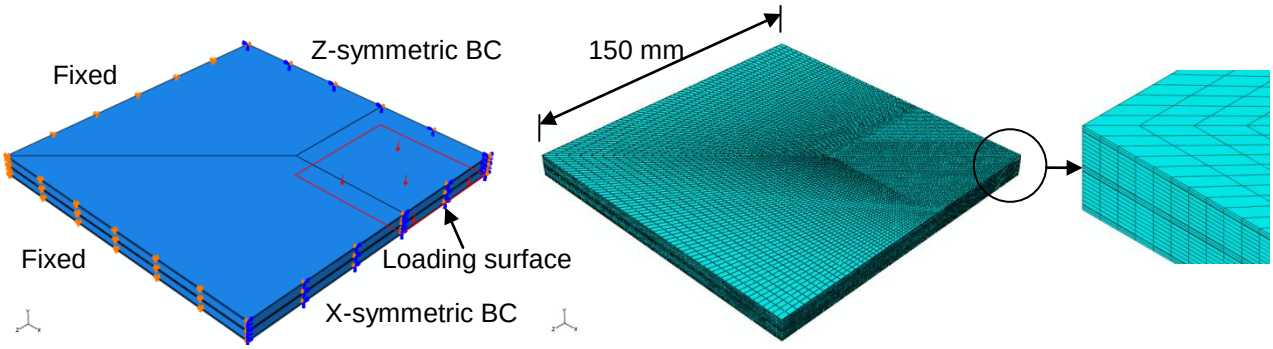

Figure 3: Dimensions, loading, boundary conditions and mesh generation for typical 3/2 FML panel.

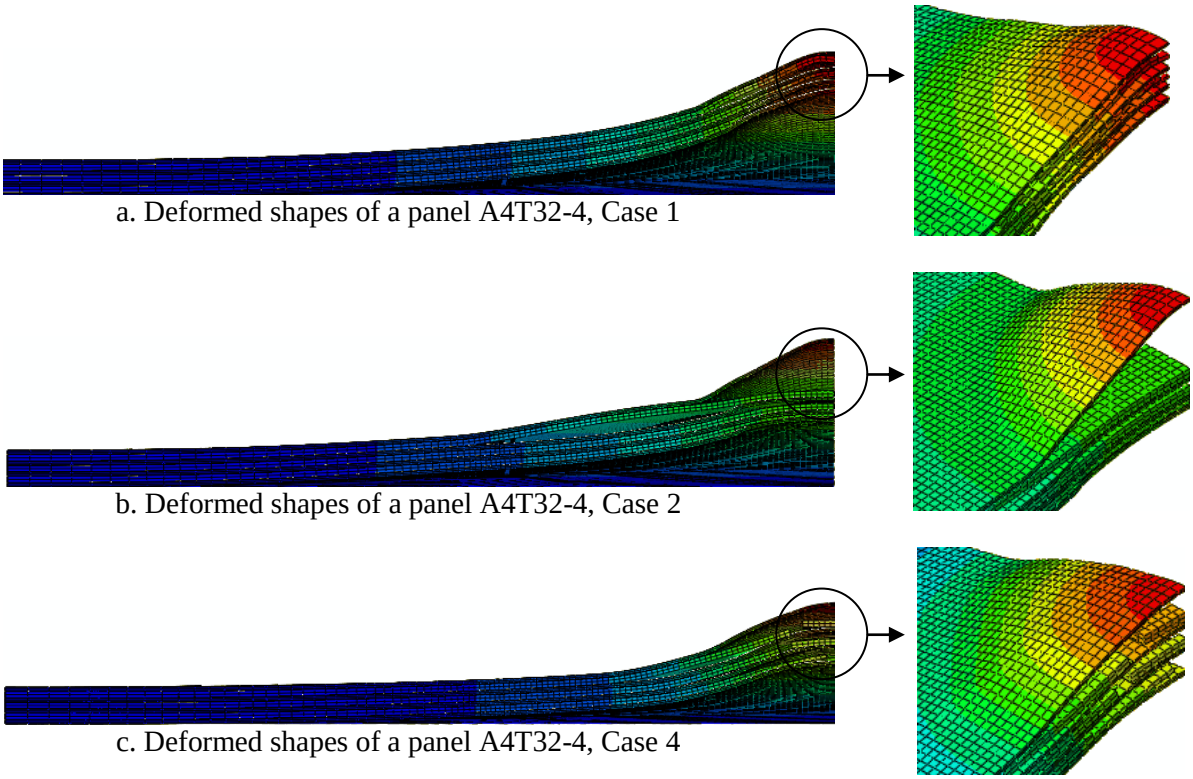

a. Deformed shapes of a panel A4T32-4, Case 1

b. Deformed shapes of a panel A4T32-4, Case 2

c. Deformed shapes of a panel A4T32-4, Case 4

Figure 4: Deformed shapes of a panel A4T32-4 with different model of strain-rate.

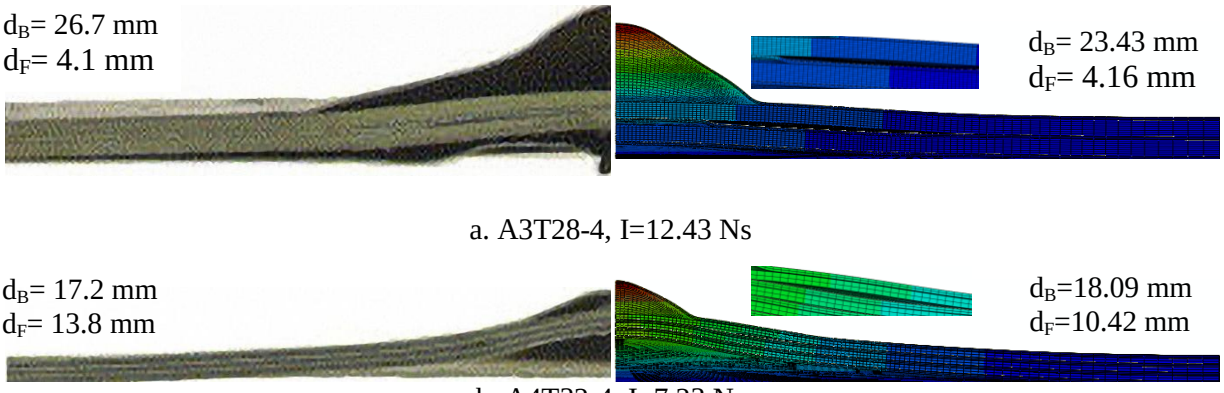

a. A3T28-4, I=12.43 Ns

b. A4T32-4, I=7.23 Ns

Figure 5: Comparison between the experiments and numerical simulations of panels A3T28-4 and T4T32-4.

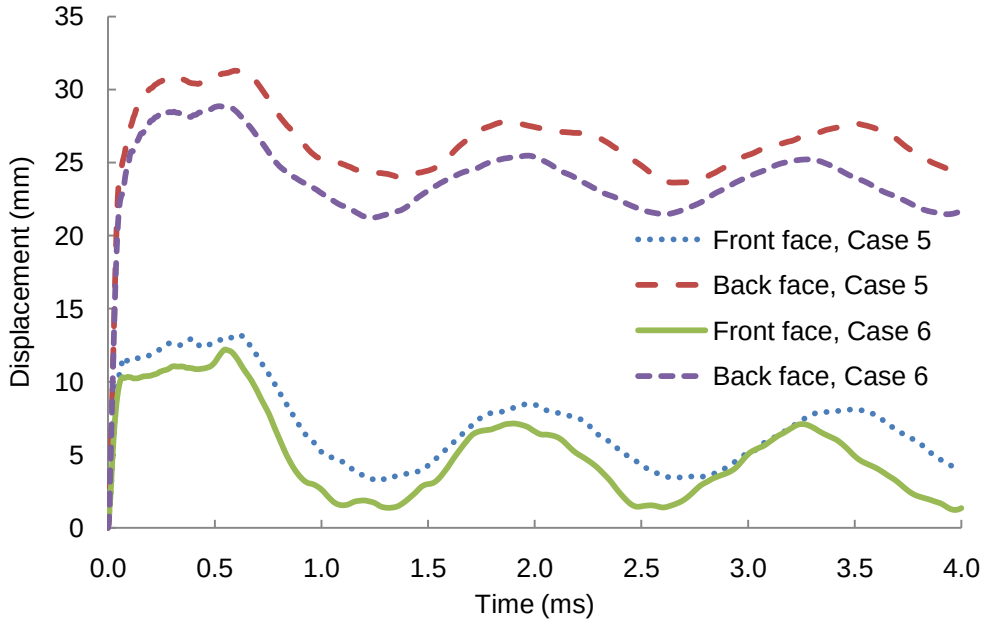

a. A3T28-4, I=12.43 Ns

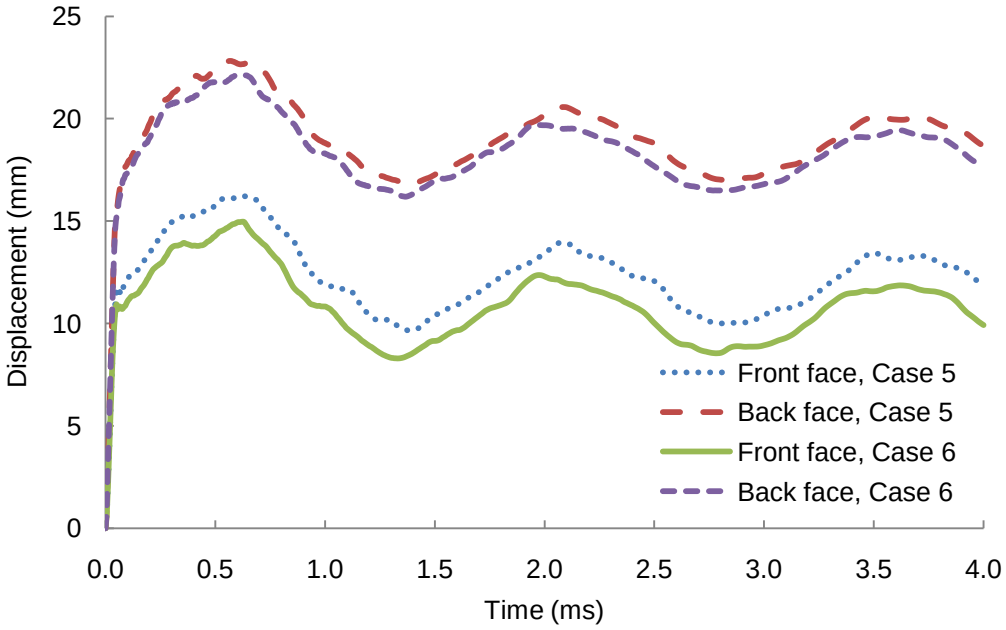

b. A4T32-4, I=7.23 Ns

Figure 6: Front and back displacement versus time for panels A3T28-4 and A4T32-4 with two models of strain-rate.

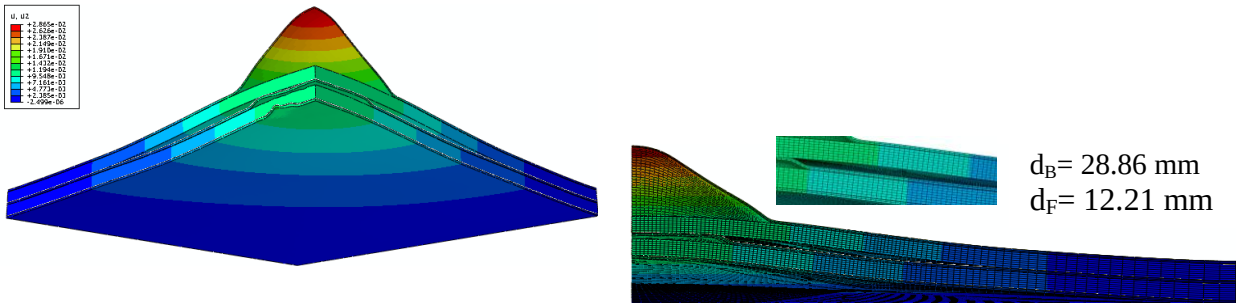

a. Transient displacement of a panel A3T28-4, frame taken close to the transient maximal deflection, after 0.52 ms

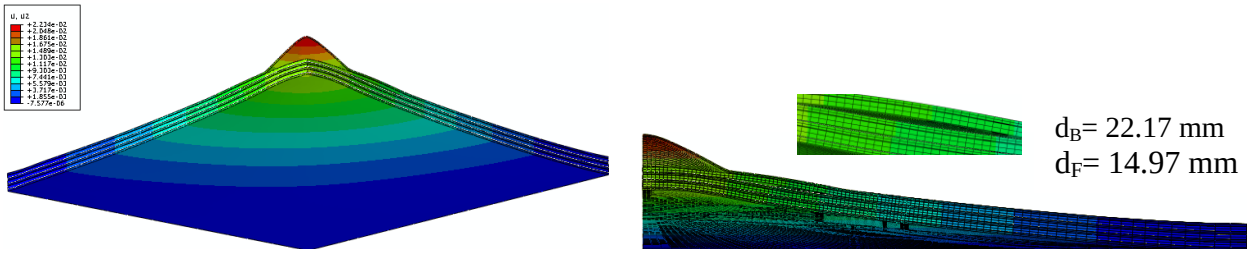

b. Transient displacement of a panel A4T32-4, frame taken close to the transient maximal deflection, after 0.60 ms

Figure 7: Transient displacement of panels A3T28-4 and T4T32-4.

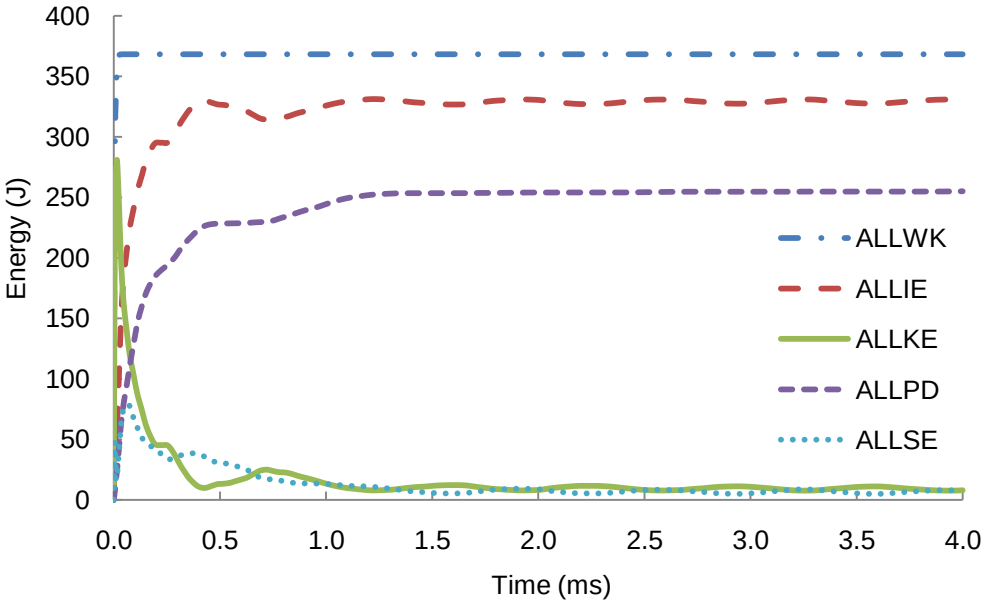

a. A3T28-4, I=12.43 Ns

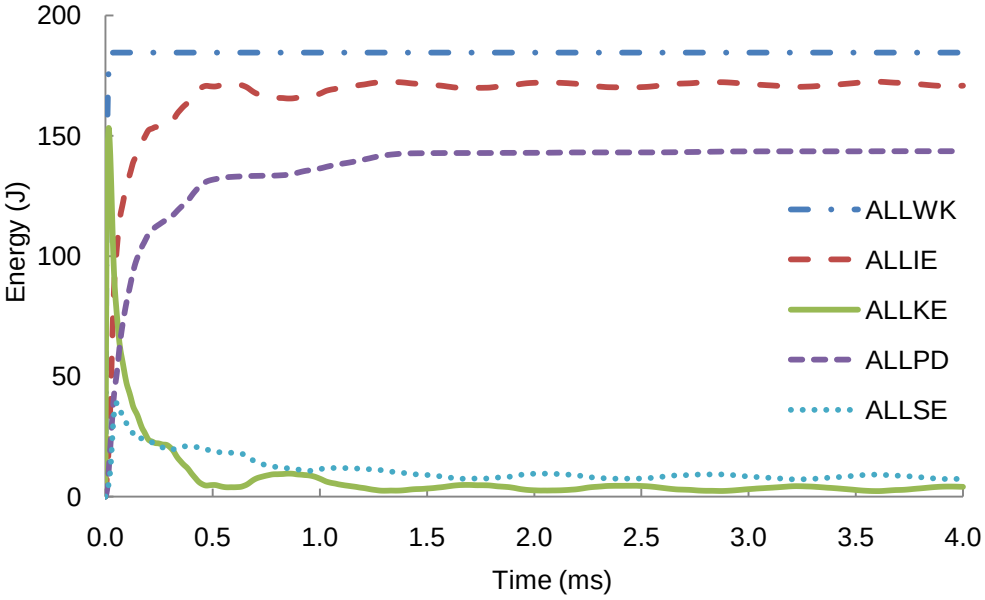

b. A4T32-4, I=7.23 Ns

Figure 8: The time history of the energies of panels A3T28-4 and T4T32-4.

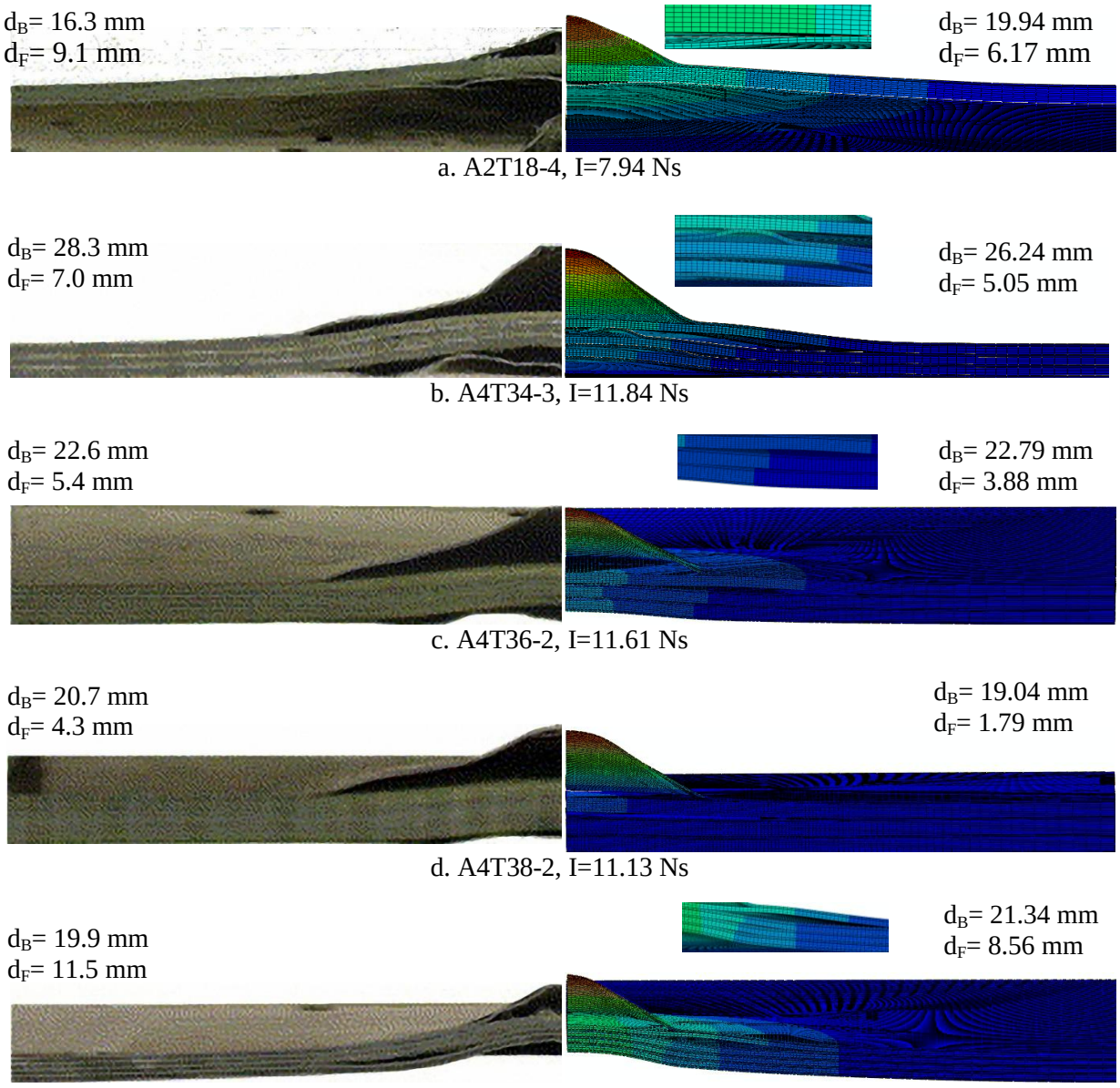

Figure 9: Comparison between the experiments and numerical simulations of panels A2T18-4, A4T34-3, A4T36-2, A4T38-2 and T5T42-4.

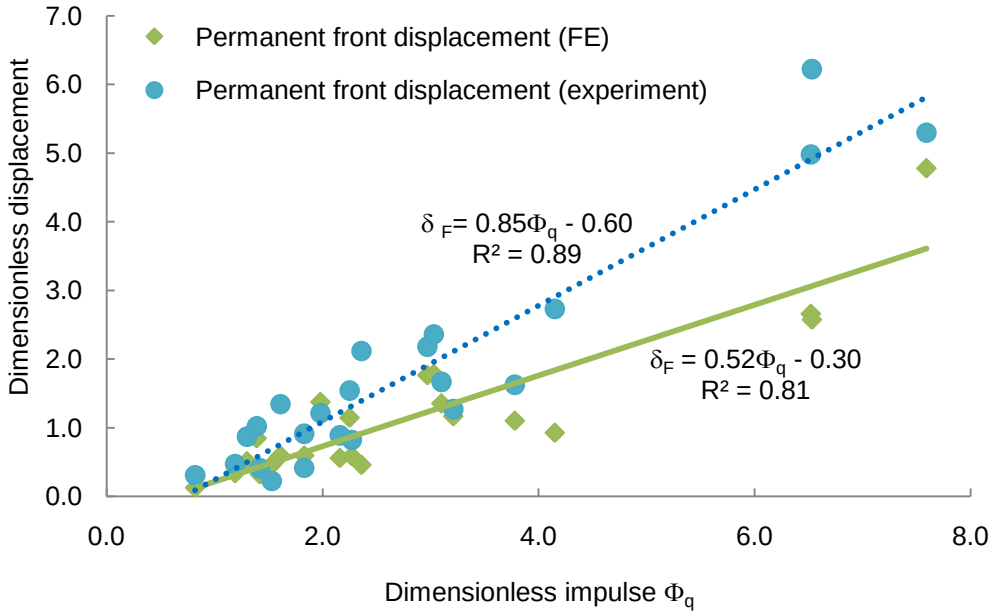

Figure 10: Graph of non-dimensional permanent displacement of front face versus non-dimensional impulse.

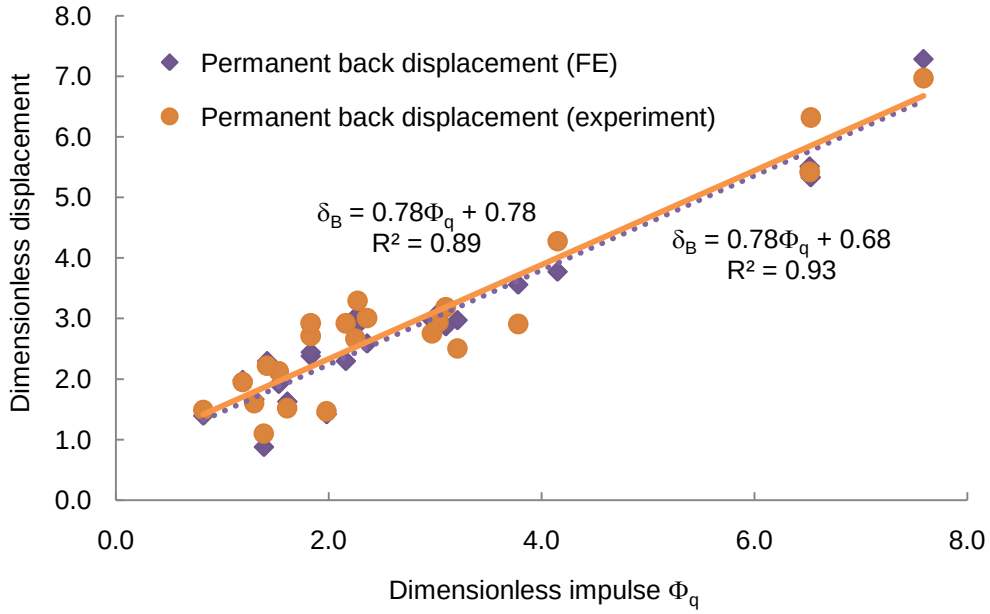

Figure 11: Graph of non-dimensional permanent displacement of back face versus non-dimensional impulse.

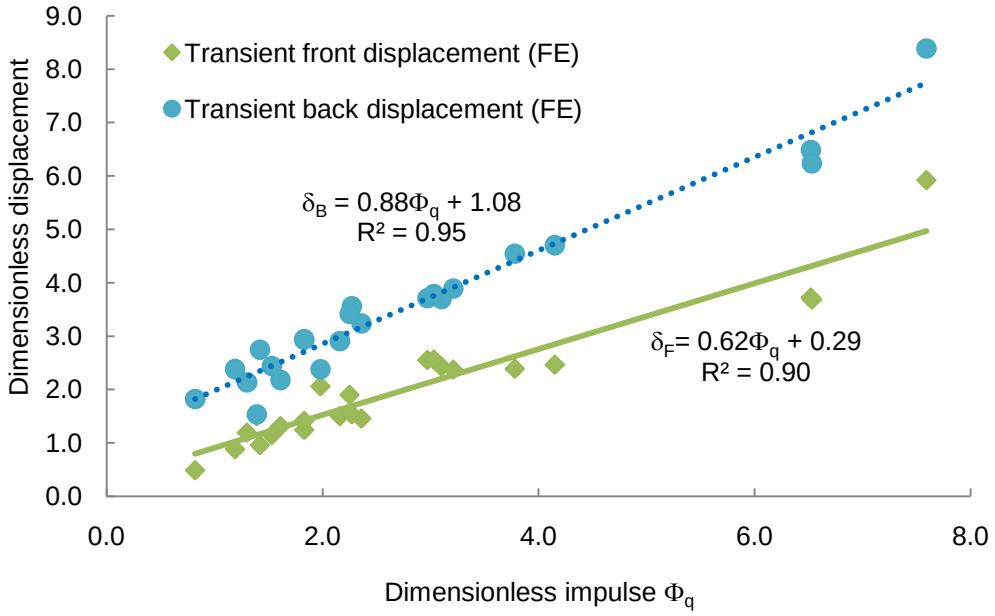

Figure 12: Graph of non-dimensional transient displacement of back and front face versus non-dimensional impulse.